Supporting Information

Photonic Multitasking Interleaved Si Nanoantenna Phased Array

Dianmin Lin[1,2], Aaron L. Holsteen[1], Elhanan Maguid[3], Gordon Wetzstein[2], Pieter G. Kik[4], Erez Hasman[3], Mark L. Brongersma[1*]

1. Geballe Laboratory for Advanced Materials, Stanford University, Stanford, California 94305, USA
2. Department of Electrical Engineering, Stanford University, Stanford, California 94305, USA
3. Micro and Nanooptics Laboratory, Faculty of Mechanical Engineering and Russell Berrie Nanotechnology Institute, Technion–Israel Institute of Technology, Haifa 32000, Israel
4. CREOL, The College of Optics and Photonics, University of Central Florida, Florida 32816, USA

* To whom correspondence should be addressed. E-mail: brongersma@stanford.edu.

S1. Diameter and intensity of focal spots of multifunctional metasurface lens

The focal spots generated by a multifunctional metasurface lens (MML) are compared to those generated by a single full metasurface lens of the same diameter. The calculated intensity profile of the transmitted beam at a wavelength of 550 nm and based on the Fresnel approximation is shown in Fig. S1. The focal spot of the multifunctional metasurface lens (Fig. S1b-c) at focal plane of 100 μm are seen to feature a spot size with full width at half maximum (FWHM) of 640 nm that is equal to that of the single lens (Fig.S1e-f). In experiment, the focal spot of MML measures FWHM of 683 nm at an illumination wavelength of 550 nm at the focal plane 100 μm behind the MML, which agrees well with optical simulations. By utilizing our multiplexing method, the diameter of each sub-lens within multifunctional metasurface lens is equal to that of a single lens, thus each MML has the same effective numerical aperture as the single full lens. Therefore, the multiplexed multifunctional metasurface lens shows an enhanced numerical aperture as compared to spatially separated multifunctional optical elements, where the lens area for each individual lens scales as $1/N_c$ with N_c the number of sublenses, resulting in a reduced N.A. for each sublens. This approach has the advantage of adding multiple optical functionalities without compromising spatial resolution.
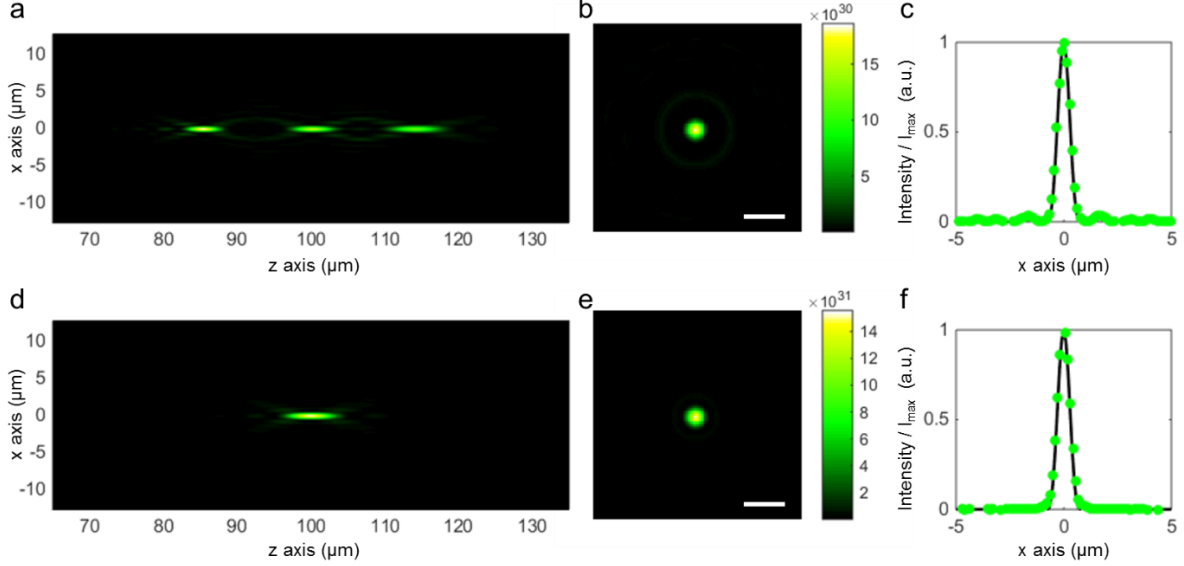
Fig. S1. (a) Simulated intensity profile behind the multifunctional metasurface lens in the x-z plane. (b) Simulated two-dimensional intensity profile in the focal plane of z=100 μm. The scale bar is 2 μm. (c) Simulated (continuous line) and measured (solid circles) cross sectional intensity profile through the focus along the x axis at the focal plane. (d) Simulated intensity profile behind the single full metasurface lens in the x-z plane. (e) Simulated two-dimensional intensity profile in the focal plane at z=100 μm. The scale bar is 2 μm. (f) Simulated (continuous line) and measured (solid circles) cross sectional intensity profile through the focus along the x axis at the focal plane.

One limitation of spatially multiplexed optical elements with a shared aperture is seen in the corresponding loss in amplitude of the focused light. The maximum intensity of each focal spot is attenuated by a factor $1/N_c^2$ compared to a full single lens at same focal spot. As shown in Fig. S1b, the maximum intensity for the three-function multiplexed ML I_{MML} is equal to 0.12 I_0, where I_0 is the maximum intensity of focal spot of non-multiplexed ML. The ratio between I_{MML} and I_0 is close to what is theoretically predicted: $1/N_c^2 = 1/9 = 0.111$. The integrated power of the main-lobe of focal spot P_{MML} is equal to 0.12 P_0, where P_0 is the integrated power of the main-lobe of focal spot of a non-multiplexed metasurface lens. However, the integrated power of the MML at focal plane P_{MML} including all the background speckle, is equal to 0.31 P_0, where P_0 is the integrated power at the focal plane of a non-multiplexed metasurface lens. The missing power in the focal spot in the case of MML is redistributed in background speckle. For imaging systems, especially microscopes, the achievement of a high spatial resolution image is often more important than achieving a high brightness image, which can often be mitigated by increasing the intensity of the light source or the imaging integration time.

S2. Strategy for spatial multiplexing

A spatially multiplexed multifunctional metasurface lens can achieve multiple optical functions within a shared surface region or aperture. The design of a MML begins with choosing the phase profiles of multiple desired optical elements that are to be included. The phase profiles of each

element are then spatially segmented. The different phase profiles belonging to the different optical elements are then spatially interleaved by removing segments from each phase profile and combining the remaining segments into a non-overlapping combined phase profile that completely fills the available surface area. Each phase profile in the resulting spatially multiplexed metasurface is given an equal area/weight.

In the process of spatially multiplexing an optical element, many choices can be made for the size and shape of the sub-sections. In Fig.1c, we first divide each concentric ring into 32 equally-sized pieces, and then we randomly choose one third of the area in each ring from each original lens. We then multiplex them by superposing the complementary parts of each of the three original lenses to create a single, multi-wavelength lens that fills the entire surface area. The divided segments are randomly chosen and are given a random tangential offset to minimize diffractive effects typically seen for periodic patterns. The size of the fixed-phase segments could in principle be varied between the size of the original lens and the size of the individual building blocks (the Si nanobeams). However, for very small segments the grain boundaries between the sub-sections with different nanobeam orientations result in an ill-defined phase, resulting in a deviation from the designed phase pattern and a reduced focusing efficiency. Having very few sub-elements on the other hand results in an under-representation of certain functional elements and an over-representation of others in certain spatial regions of a composite optical element. This again leads to a performance degradation of the composite optical element. Here, we have chosen a reasonable compromise and divided the lens into 5536 parts with roughly equal area of approximately 1 μm^2.

In addition to the randomized tangential offsets of the segments described above, we also investigated other spatial multiplexing choices. We found that when the lens is divided into random placed square segments in a checkerboard pattern, the metasurface lens could achieve wavefront shaping with improved imaging and focusing properties. However, we also found that for lenses divided into segments that are smaller than approximately 200 nm × 200 nm, the maximum intensity drops significantly, as shown in Fig. S2. This is attributed to the fact that the segments feature only very few Si nanobeams, and each segment no longer serves as a waveplate, as assumed in the optical design. In this case the coupling between antennas of different orientation needs to be taken into account.
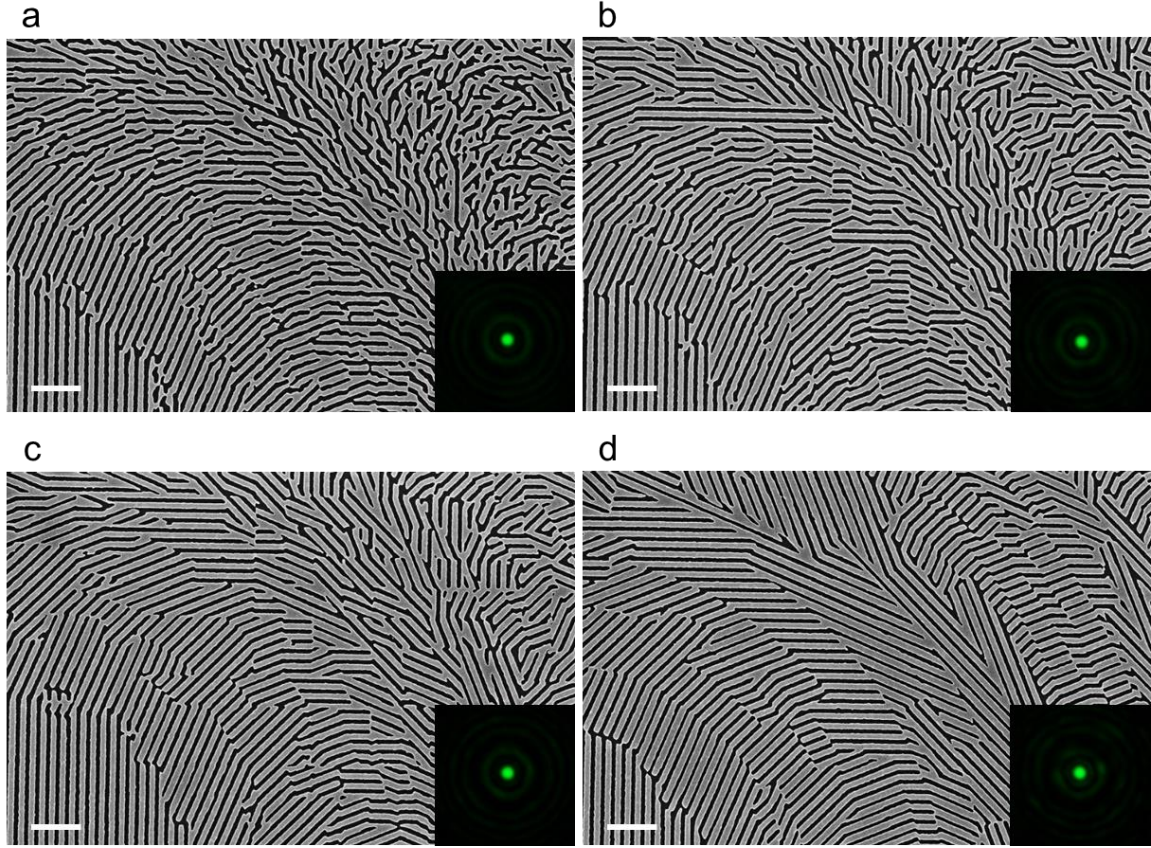
Fig. S2. Scanning electron microscopy images of MMLs with different multiplexing schemes (a) pixel of 200 nm × 200 nm; (b) pixel of 400 nm × 400 nm; (c) pixel of 600 nm × 600 nm; (d) segmented concentric rings. The scale bar is 1 μm. The focal spot generated by each MML design is shown in the inset.

S3. Imaging using a metasurface lens

Imaging using a conventional lens is shown schematically in Fig. S3a. The distance s_1 between the object and the conventional lens and the distance s_2 between the lens and the images follows from the lens equation. Imaging using a metasurface lens is shown schematically in Fig. S3b. A single non-multiplexed metasurface lens can act as a single lens imaging system. For a ML based on the geometric phase, the lens acts as a positive or negative lens depending on the helicity of the incident light. For left-circularly polarized (LCP) light, the fabricated metasurface lens serves as a positive lens which causes the light from the object to refocus at an image plane on the transmission side of the lens, forming a real, inverted image of the object. The object and image distances s_1 and s_2 follow the lens equation, with a modification due to the presence of a planar glass substrate. The image magnification can be varied as in traditional single-lens imaging by adjusting the distance between object and the metasurface lens. The real image generated by a metasurface lens can be directly captured by a CCD placed in the focal plane. In the present study the size of metasurface lens is small in order to limit the fabrication time, and combined with the small focal length the size of the resulting images is on the micrometer scale. The

generated image is therefore magnified using an optical microscope and projected onto a CCD camera.
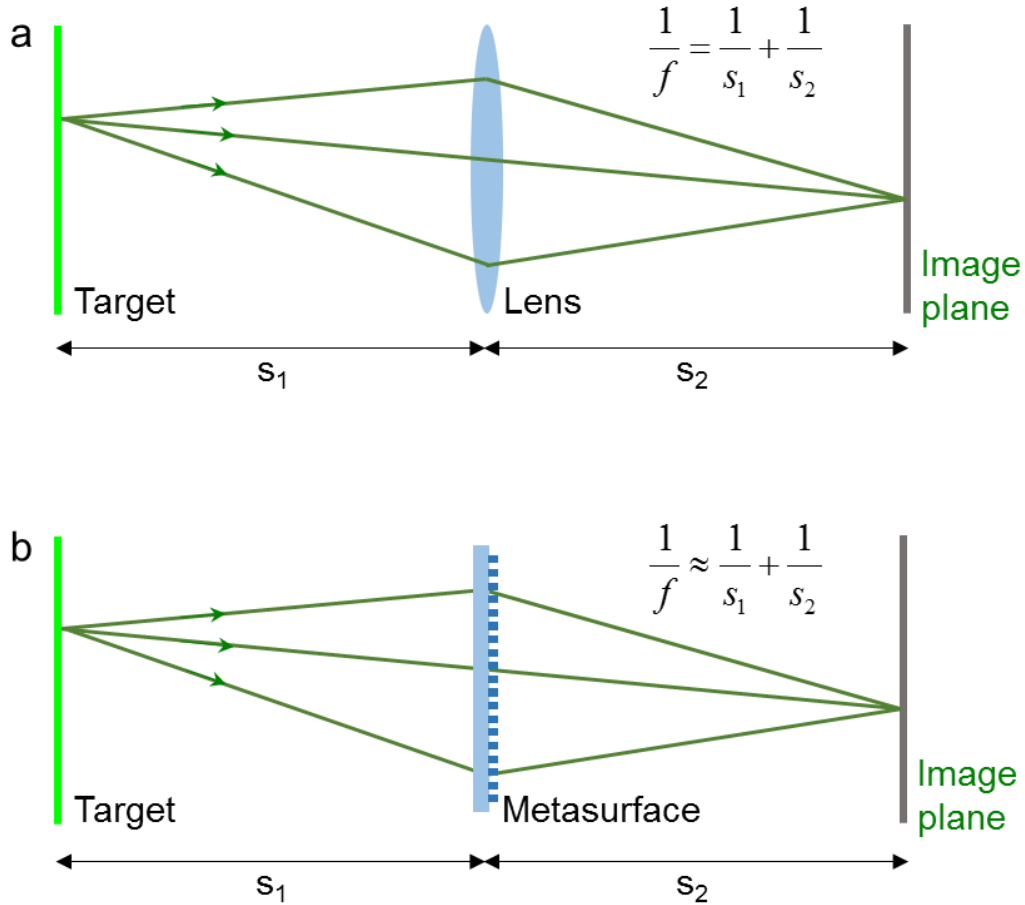
Fig. S3 (a) Schematic of imaging using a conventional lens. (b) Schematic of imaging using a metasurface lens illuminated with left-circularly polarized light.

S4. Imaging using a single metasurface lens

Here we demonstrate the imaging properties of a single non-multiplexed metasurface lens with a numerical aperture of 0.43 and a focal length of 100 μm. Figure S4a shows a white-light reflection optical microscopy image of the lens, which appears blue-green. A Thorlabs 1951 USAF resolution target back-illuminated by a tunable laser source is used as the object. The imaged region contains the number 7 and slits with a line width of 4.3 μm and periodicity of 7.8 μm. The optical microscopy image of the target is shown in Fig. S4b. For incident LCP light the fabricated metasurface lens acts as a positive lens that forms a real, inverted image at an image plane on the transmission side of the lens. Using a microscope objective to probe the image plane of the metasurface lens, we detect the inverted image of the target created by the metasurface lens in Fig. S4c. When the object is illuminated with right circularly polarized (RCP) light, the

metasurface lens acts as a negative lens that generates a virtual image on the object side, as shown in Fig. S4d. Consistent with the theoretical calculation of the spatial resolution for a lens of this N.A., we are able to easily resolve these micron-sized features.
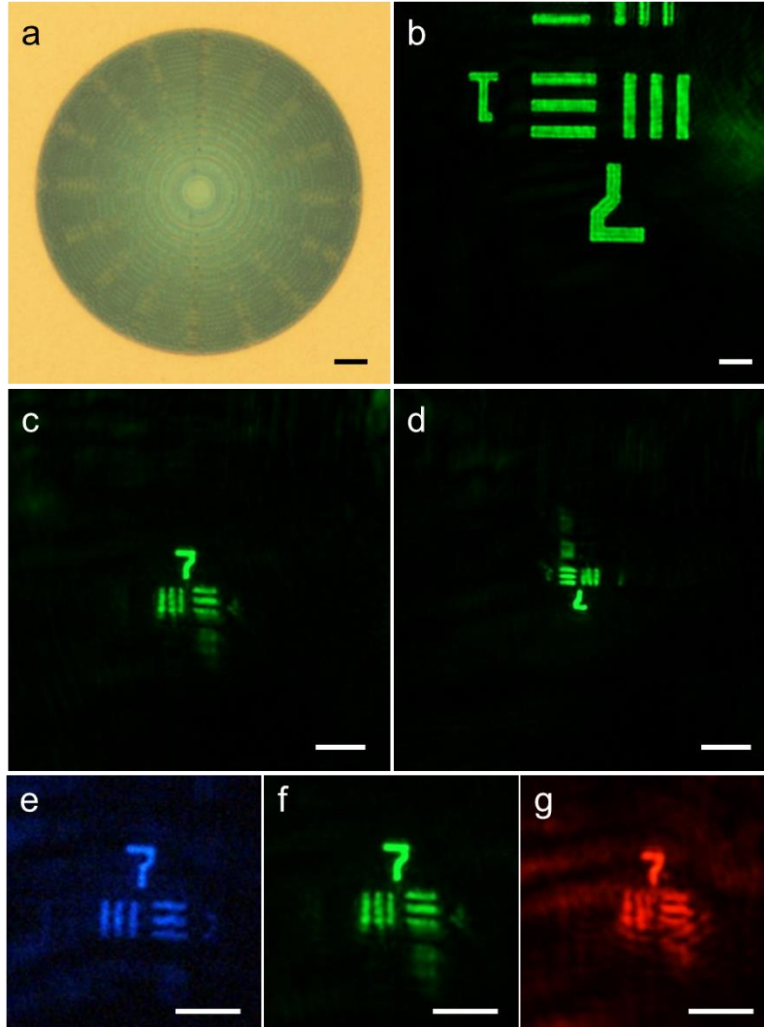
Fig. S4. (a) The reflection optical microscopy image of a non-multiplexed metasurface lens. (b) The transmission optical microscopy image of resolution target under 20× magnification. Generated images by the metasurface lens with (c) positive focal length and thus real image respectively, and (d) negative focal length and thus virtual image. (e-g) Images regenerated by metasurfaces upon different color illumination at wavelength of 480nm, 550nm, and 620nm respectively. The scale bar is 10 μm.

The metasurface lens in Fig. S4 was designed for optimal focusing of green light with a wavelength of 550 nm. When the object is illuminated with a different wavelength, such as red or blue, images are formed at different distances from the metasurface lens and with different magnification due its chromatic dispersion properties, (See Fig. S4e-g). The image quality and

efficiency would also be wavelength-dependent. The zeroth-order diffraction (transmitted laser beam without encoded phase information) would add a background signal with opposite helicity to that of the 1st order diffraction (encoded with phase) and is therefore filtered out by adding a quarter waveplate and a linear polarizer before the CCD. In the measurements shown in Fig. S4c-g, no circular polarizer was added before the CCD and consequently a background signal is present caused by the 0th order diffraction, the strength of which depends on the first-order diffraction efficiency of the metasurface lens. For a wavelength of 620 nm, the metasurface has a lower ratio between the image-forming diffracted light and the transmitted zeroth-order contribution, therefore there is more background signal in Fig. S4g. Note that at shorter wavelength (blue image) a higher spatial resolution is achieved, as expected.

S5. Schematics of imaging using multifunctional metasurface lenses

Figure S5 shows the schematic of the imaging systems for the two multifunctional metasurface lenses discussed in the manuscript. The imaging system with the interleaved multifunctional metasurface lenses can be approximated as a superposition of multiple metasurface sublenses. In one of our designs, the three sublenses featured a shared focal length of 100 μm at three different wavelengths respectively. We are interested in the image plane corresponding to the focal length of 100 μm.

The axial MML has a shared optical axis for the three sublenses and therefore focuses RGB light to the same focal spot. Figure S5a shows in a schematic how this MML is used for imaging purposes. For clarity, only the rays corresponding to the focal length of 100 μm are plotted in the figure. After the light passes through the axial MML the chosen phase profile ensures that RGB colors come into focus at the same location in the image plane corresponding to a focal length of 100 μm.

The imaging schematic for the color separating MML is shown in supplementary Fig. S5b. Again only the rays corresponding to the designed focal length of 100 μm are shown in the figure. After the light passes through the color separating MML, we expect that at the image plane corresponding to the focal length of 100 μm, RGB colors will come into focus onto the same image plane, but with RGB colors steered to different lateral positions within the image plane.
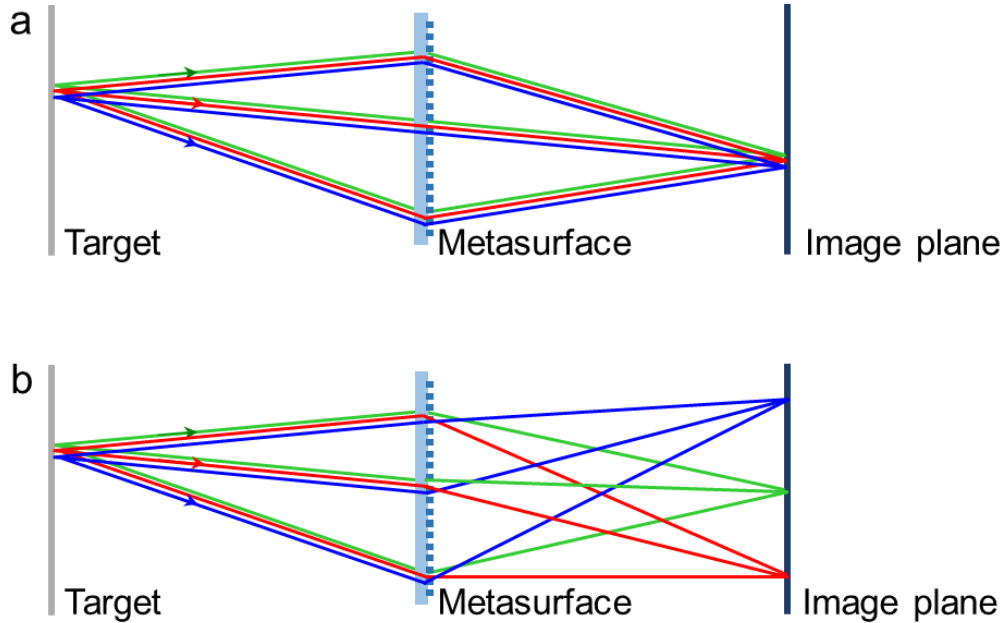
Fig. S5. (a) Schematic of the imaging system of the axial MML, which focus RGB colors at the same location in the shared image plane. (b) Schematic of the imaging system of the color separating MML, which separates different colors at different locations on the shared imaging plane.

S6. Images generated by axial MML

We have demonstrated multi-wavelength imaging with the axial MML design (Fig. 1 and 2 and Fig. S5). The optical microscopy image of an axial MML is shown in Fig. S6a. The axial MML will project RGB colors onto the shared image plane without color separation. Here, we choose RGB pixels from a cell phone LCD screen as the object, as shown in the conventional optical microscopy image in Fig. S6a. It contains RGB pixels within the same plane and the size of each pixel is on the order of 20 μm, smaller than the diameter of the MML. When light from the LCD screen passes through the axial MML, which can be approximated as a superposition of three sub-lenses with a common optical axis, each sub-lens focuses the LCP component of each color channel to the shared image plane (Fig. S5a). The resulting image is captured by a microscope objective (Fig. S6c). The MML is seen to image the three differently colored pixels onto the same image plane corresponding to a focal length of 100 μm and the resulting image is inverted as expected. Due to the presence of a thick glass cover on the LCD screen, the MML is located about 1 mm away from the object, and therefore the image generated by MML is de-magnified by a factor of 6. Although the RGB pixel array is very large compared to the metasurface lens, only the pixels within the field of view of the metasurface lens are imaged and shown in the refocused image (See Fig. S6c-e). For pixels further from the axis of lens, the off-axis aberration is more severe, resulting in a reduced brightness and resolution at the edge of the image. The emitted light from the LCD display is linearly polarized, and consequently only half of the light (the LCP component) comes into focus and generates the image, while the light with the opposite polarization results in the background signal in the image.

In addition to the image plane shown in Fig. S6c, there are other image planes corresponding to additional focal lengths. Figure S6d shows the image generated by this axial MML at the image plane corresponding to the focal length of 87 μm, where red and green pixels are focused by the sublenses designed for blue and green light respectively. Figure S6e shows the image at the image plane corresponding to the focal length of 117 μm, where blue and green pixels are focused by the sublenses designed for green and red light respectively. The magnification of the images is different at different image planes, because the corresponding focal lengths are different. In addition, in this case these additional image planes are far away with respect to the microscope's depth of focus. For this reason, these additional image planes cannot be seen in Fig. S6c.
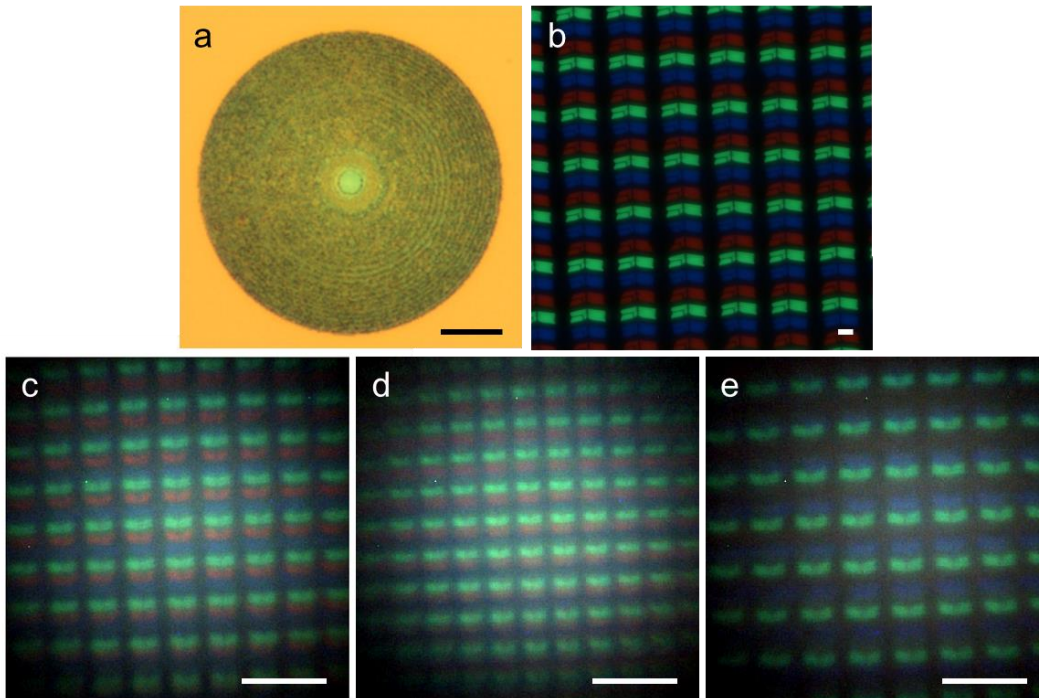
Fig. S6 (**a**) Optical microscope images of the axial MML. (**b**) a target (iPhone 6) emitting RGB colors from the same plane, and (**c**) image formed by the axial MML at a shared image plane corresponding to focal length of 100 μm. Image generated by this MML at other image planes (**d**) where red and green are focused on the same image plane and (**e**) where green and blue are focused on the same image plane. The scale bar is 20 μm.

S7. Images generated by the color separating MML

The optical microscopy image of a color separating MML is shown in Fig. S7a. This MML separates different colors at different locations on the shared imaging plane. The original image generated by the color separating MML is shown in Fig. S7b. Some degree of spatial and chromatic crosstalk occurs between the different color channels, which can be filtered out as described in the following. Figure 5c shows the image after filtering out spurious signal from additional color channels.

There is crosstalk between the different imaging planes due to the chromatic dispersion that is present within each sub-lens. For example, the image plane corresponding to a focal length of 87 µm will produce a background signal at the image plane corresponding to the focal length of 100 µm. As a result, a blue and green speckle pattern is present on the red 'S' image, which can be filtered out by simple image processing. The individual detected RGB images associated with the color channels in Fig. S7b are plotted respectively in Fig. S7c-e. This separation into R, G, and B channels largely removes the speckle caused by other sublenses and colors. For instance, the blue and green speckle on top of the red 'S' seen in Fig. S7b is absent from the red channel shown in Fig. S7c. Note that a red speckle is still visible at the center of Fig. S7c. In the final image Fig. 5c this image portion has been removed by limiting the field of view to the region of the S only. In practice this means that the field of view will be related by the lateral color displacement in this color-separating MML. A similar field-of-view reduction was done for the blue and green channels. Finally a small cross-talk contribution was removed from the green channel. The design wavelength for the blue color of the color separating MML is 480 nm, which does not exactly match the peak wavelength of the color filter on the color CCD used here. Therefore, light with a wavelength of 480 nm will cause a small signal contribution in the green color channel, as seen in Fig. S7d. This type of cross-talk can be avoided in practice by more precisely matching the filter response with the design wavelength. In Figure 5c, this small blue-green cross-talk contribution was subtracted from the green image. The multifunctional metasurface lens combined with simple post-processing allows imaging and color separation using a single MML, which could not have been achieved by a single traditional optical element.
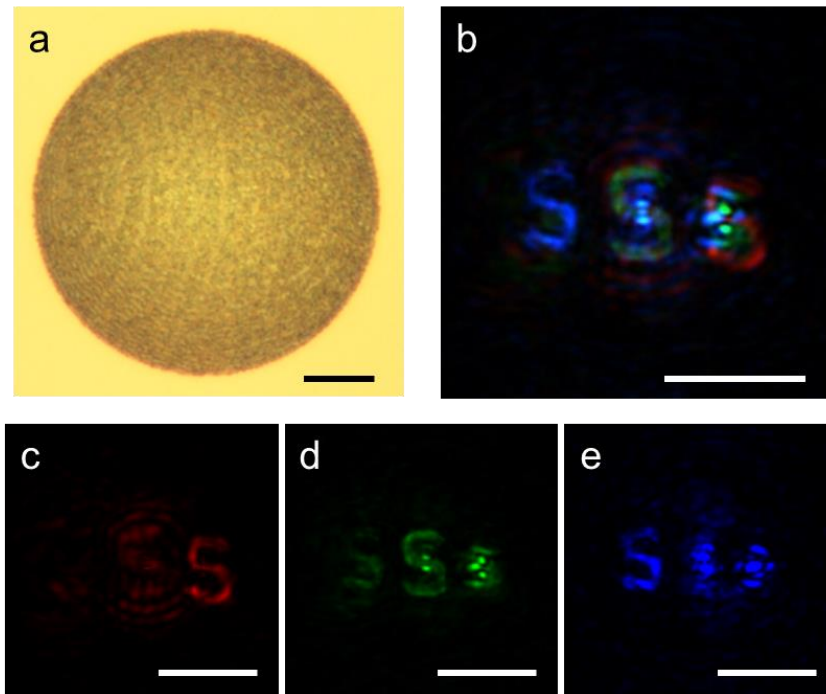
Fig. S7 (a) Optical microscopy image of a color separating MML. **(b)** Original image generated by this MML at the shared image plane. **(c-e)** The RGB color channels of digital image in **(b)** are plotted respectively. The scale bar is 20 µm.

REFERENCES

REFERENCES

1. Bomzon, Z., Kleiner, V. & Hasman, E. Pancharatnam-Berry phase in space-variant polarization-state manipulations with subwavelength gratings. *Opt. Lett.* **26,** 1424–1426 (2001).
2. Bomzon, Z., Biener, G., Kleiner, V. & Hasman, E. Space-variant Pancharatnam–Berry phase optical elements with computer-generated subwavelength gratings. *Opt. Lett.* **27,** 1141–1143 (2002).
3. Lalanne, P., Astilean, S., Chavel, P., Cambril, E. & Launois, H. Blazed binary subwavelength gratings with efficiencies larger than those of conventional échelette gratings. *Opt. Lett.* **23,** 1081–1083 (1998).
4. Lalanne, P., Astilean, S., Chavel, P., Cambril, E. & Launois, H. Design and fabrication of blazed binary diffractive elements with sampling periods smaller than the structural cutoff. *J. Opt. Soc. Am. A* **16,** 1143–1156 (1999).
5. Verslegers, L., Catrysse, P. B., Yu, Z. F., White, J. S., Barnard, E. S., Brongersma, M. L. & Fan, S. H. Planar Lenses Based on Nanoscale Slit Arrays in a Metallic Film. *Nano Lett.* **9,** 235–238 (2009).
6. Ni, X. J., Emani, N. K., Kildishev, A. V, Boltasseva, A. & Shalaev, V. M. Broadband Light Bending with Plasmonic Nanoantennas. *Science* **335,** 427 (2012).
7. Pors, A., Albrektsen, O., Radko, I. P. & Bozhevolnyi, S. I. Gap plasmon-based metasurfaces for total control of reflected light. *Sci. Rep.* **3,** 2155 (2013).
8. Yu, N. F., Genevet, P., Kats, M. A., Aieta, F., Tetienne, J. P., Capasso, F. & Gaburro, Z. Light Propagation with Phase Discontinuities: Generalized Laws of Reflection and Refraction. *Science* **334,** 333–337 (2011).
9. Lin, D. M., Fan, P. Y., Hasman, E. & Brongersma, M. L. Dielectric gradient metasurface optical elements. *Science* **345,** 298–302 (2014).
10. Chong, K. E., Staude, I., James, A., Dominguez, J., Liu, S., Campione, S., Subramania, G. S., Luk, T. S., Decker, M., Neshev, D. N., *et al.* Polarization-Independent Silicon Metadevices for Efficient Optical Wavefront Control. *Nano Lett.* **15,** 5369–5374 (2015).
11. Veksler, D., Maguid, E., Shitrit, N., Ozeri, D., Kleiner, V. & Hasman, E. Multiple Wavefront Shaping by Metasurface Based on Mixed Random Antenna Groups. *ACS Photonics* **2,** 661–667 (2015).
12. Maguid, E., Yulevich, I., Veksler, D., Kleiner, V., Brongersma, M. L. & Hasman, E. Photonic spin-controlled multifunctional shared-aperture antenna array. *Science* **352,** 1202–1206 (2016).
13. Hasman, E., Kleiner, V., Biener, G. & Niv, A. Polarization dependent focusing lens by use of quantized Pancharatnam-Berry phase diffractive optics. *Appl. Phys. Lett.* **82,** 328–330 (2003).
14. Fattal, D., Li, J. J., Peng, Z., Fiorentino, M. & Beausoleil, R. G. Flat dielectric grating reflectors with focusing abilities. *Nat. Photonics* **4,** 466–470 (2010).
15. Ishii, S., Kildishev, A. V, Shalaev, V. M., Chen, K.-P. & Drachev, V. P. Metal nanoslit lenses with polarization-selective design. *Opt. Lett.* **36,** 451–453 (2011).
16. Arbabi, A., Horie, Y., Ball, A. J., Bagheri, M. & Faraon, A. Subwavelength-thick lenses

with high numerical apertures and large efficiency based on high-contrast transmitarrays. *Nat. Commun.* **6,** 7069 (2015).

17. Khorasaninejad, M., Chen, W. T., Devlin, R. C., Oh, J., Zhu, A. Y. & Capasso, F. Metalenses at visible wavelengths: Diffraction-limited focusing and subwavelength resolution imaging. *Science* **352,** 1190–1194 (2016).

18. Bomzon, Z., Biener, G., Kleiner, V. & Hasman, E. Radially and azimuthally polarized beams generated by space-variant dielectric subwavelength gratings. *Opt. Lett.* **27,** 285–287 (2002).

19. Zeng, J., Gao, J., Luk, T. S., Litchinitser, N. M. & Yang, X. Structuring Light by Concentric-Ring Patterned Magnetic Metamaterial Cavities. *Nano Lett.* **15,** 5363–5368 (2015).

20. Shitrit, N., Bretner, I., Gorodetski, Y., Kleiner, V. & Hasman, E. Optical Spin Hall Effects in Plasmonic Chains. *Nano Lett.* **11,** 2038–2042 (2011).

21. Yin, X., Ye, Z., Rho, J., Wang, Y. & Zhang, X. Photonic Spin Hall Effect at Metasurfaces. *Science* **339,** 1405–1407 (2013).

22. Ni, X., Kildishev, A. V & Shalaev, V. M. Metasurface holograms for visible light. *Nat. Commun.* **4,** 2807 (2013).

23. Zheng, G., Mühlenbernd, H., Kenney, M., Li, G., Zentgraf, T. & Zhang, S. Metasurface holograms reaching 80% efficiency. *Nat. Nanotechnol.* **10,** 308–312 (2015).

24. Segal, N., Keren-zur, S., Hendler, N. & Ellenbogen, T. Controlling light with metamaterial-based nonlinear photonic crystals. *Nat. Photonics* **9,** 180–184 (2015).

25. Sautter, J., Staude, I., Decker, M., Rusak, E., Neshev, D. N., Brener, I. & Kivshar, Y. S. Active Tuning of All-Dielectric Metasurfaces. *ACS Nano* **9,** 4308–4315 (2015).

26. Wang, Q., Rogers, E. T. F., Gholipour, B., Wang, C.-M., Yuan, G., Teng, J. & Zheludev, N. I. Optically reconfigurable metasurfaces and photonic devices based on phase change materials. *Nat Phot.* **10,** 60–65 (2016).

27. Shalaev, M. I., Sun, J., Tsukernik, A., Pandey, A., Nikolskiy, K. & Litchinitser, N. M. High-Efficiency All-Dielectric Metasurfaces for Ultracompact Beam Manipulation in Transmission Mode. *Nano Lett.* **15,** 6261–6266 (2015).

28. Arbabi, A., Horie, Y., Bagheri, M. & Faraon, A. Dielectric metasurfaces for complete control of phase and polarization with subwavelength spatial resolution and high transmission. *Nat Nanotechnol* **10,** 937–943 (2015).

29. Biener, G., Niv, A., Kleiner, V. & Hasman, E. Formation of helical beams by use of Pancharatnam-Berry phase optical elements. *Opt. Lett.* **27,** 1875–1877 (2002).

30. Niv, A., Biener, G., Kleiner, V. & Hasman, E. Manipulation of the Pancharatnam phase in vectorial vortices. *Opt. Express* **14,** 4208–4220 (2006).

31. Chen, X. Z., Huang, L. L., Muhlenbernd, H., Li, G. X., Bai, B. F., Tan, Q. F., Jin, G. F., Qiu, C. W., Zhang, S. & Zentgraf, T. Dual-polarity plasmonic metalens for visible light. *Nat. Commun.* **3,** 1198 (2012).

32. Aieta, F., Kats, M. A., Genevet, P. & Capasso, F. Multiwavelength achromatic metasurfaces by dispersive phase compensation. *Science* **347,** 1342–1345 (2015).

33. Khorasaninejad, M., Aieta, F., Kanhaiya, P., Kats, M. A., Genevet, P., Rousso, D. & Capasso, F. Achromatic Metasurface Lens at Telecommunication Wavelengths. *Nano Lett.* **15,** 5358–5362 (2015).

34. Arbabi, E., Arbabi, A., Kamali, S. M., Horie, Y. & Faraon, A. Multiwavelength polarization-insensitive lenses based on dielectric metasurfaces with meta-molecules.

Optica **3,** 628–633 (2016).

35.   Pozar, D. M. & Targonski, S. D. A shared-aperture dual-band dual-polarized microstrip array. *IEEE Trans. Antennas Propag.* **49,** 150–157 (2001).

36.   Haupt, R. L. Interleaved Thinned Linear Arrays. *IEEE Trans. Antennas Propag.* **53,** 2858–2864 (2005).

37.   Sayeed, A. M., Member, S. & Raghavan, V. Maximizing MIMO Capacity in Sparse Multipath With Reconfigurable Antenna Arrays. *IEEE J. Sel. Top. Signal Process.* **1,** 156–166 (2007).

38.   Lager, I. E., Trampuz, C., Simeoni, M. & Ligthart, L. P. Interleaved Array Antennas for FMCW Radar Applications. *IEEE Transactions on Antennas and Propagation* **57,** 2486–2490 (2009).

39.   LeCompte, M., Shi, S. Y. & Prather, D. W. Interleaved diffractive optical element design. *Wave-Optical Syst. Eng.* **4436,** 115–122 (2001).

40.   Cao, L. Y., Fan, P. Y., Barnard, E. S., Brown, A. M. & Brongersma, M. L. Tuning the Color of Silicon Nanostructures. *Nano Lett.* **10,** 2649–2654 (2010).

41.   Cao, L. Y., White, J. S., Park, J. S., Schuller, J. A., Clemens, B. M. & Brongersma, M. L. Engineering light absorption in semiconductor nanowire devices. *Nat. Mater.* **8,** 643–647 (2009).